

*Flow patterns around two neighboring patches of emergent vegetation and possible implications for deposition and vegetation growth*

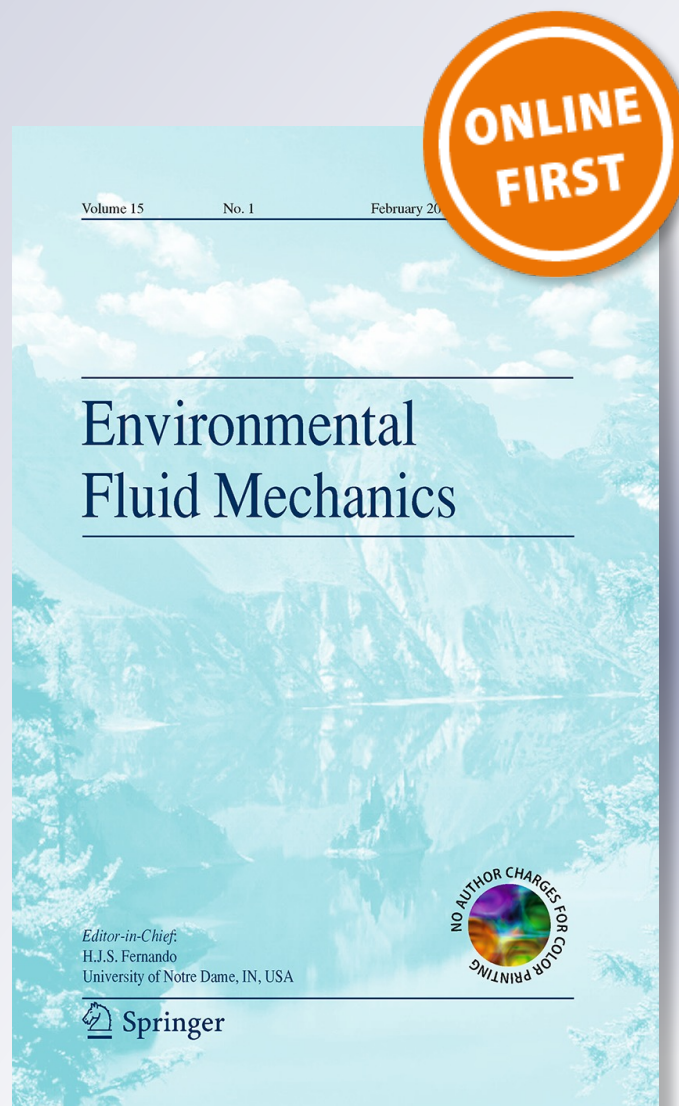
**Paulo H. S. de Lima, Johannes G. Janzen  
& Heidi M. Nepf**

**Environmental Fluid Mechanics**

ISSN 1567-7419

Environ Fluid Mech

DOI 10.1007/s10652-015-9395-2



**Your article is protected by copyright and all rights are held exclusively by Springer Science +Business Media Dordrecht. This e-offprint is for personal use only and shall not be self-archived in electronic repositories. If you wish to self-archive your article, please use the accepted manuscript version for posting on your own website. You may further deposit the accepted manuscript version in any repository, provided it is only made publicly available 12 months after official publication or later and provided acknowledgement is given to the original source of publication and a link is inserted to the published article on Springer's website. The link must be accompanied by the following text: "The final publication is available at [link.springer.com](http://link.springer.com)".**

# Flow patterns around two neighboring patches of emergent vegetation and possible implications for deposition and vegetation growth

Paulo H. S. de Lima · Johannes G. Janzen · Heidi M. Nepf

Received: 5 August 2014 / Accepted: 14 January 2015  
© Springer Science+Business Media Dordrecht 2015

**Abstract** The flow around two neighboring, circular, vegetation patches of equal diameter ( $D$ ) was investigated using computational fluid dynamics. Depending on the patches' transverse and longitudinal center-to-center spacing ( $T$  and  $L$ , respectively), several distinct flow patterns were observed. The patterns are compared to flow near an isolated patch. The key flow patterns were interpreted in terms of implications for deposition. Deposition maps were calculated for two different threshold velocities:  $0.5U_0$  and  $0.7U_0$ , where  $U_0$  is the free stream velocity. When the two patches were far away from each other, the interaction of their wakes was weak, and the flow and deposition pattern around each patch resembled that of a single, isolated patch. When the patches were very close, wake interaction took place, resulting in additional deposition along the centerline between the two patches, but further downstream than the deposition in line with each patch. For some intermediate patch spacings, the wake of the upstream patch was dramatically shortened, relative to an isolated patch, and the wake of the downstream patch was lengthened. The results show that flow distribution is influenced by interaction between neighboring vegetation patches and suggest that this may create feedbacks that influence the evolution of vegetated landscapes.

**Keywords** Sediment deposition · Landscape evolution · Patches of vegetation · Computational fluid dynamics

---

P. H. S. de Lima (✉) · J. G. Janzen  
Faculty of Engineering, Architecture and Urban Planning, and Geography, Federal University of Mato Grosso do Sul, Campo Grande, Mato Grosso do Sul, Brazil  
e-mail: paulo.lima@ufms.br

H. M. Nepf  
Department of Civil and Environmental Engineering, Massachusetts Institute of Technology, Cambridge, Massachusetts, USA

## 1 Introduction

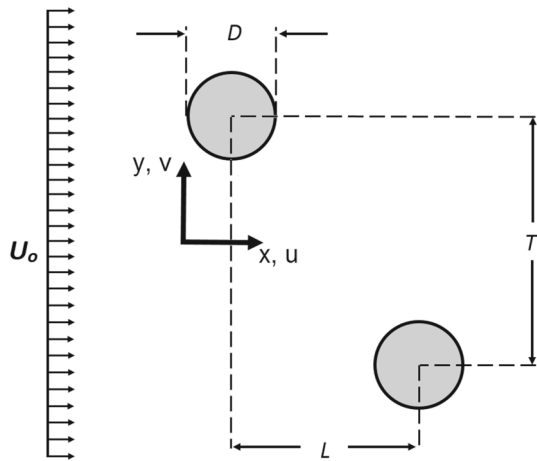
Vegetated landscapes provide a variety of ecosystem services, including providing habitat [1], producing oxygen [2], reducing turbidity [3], and decreasing bank erosion [4]. These landscapes develop over time scales of decades to millennia through the action of vegetation-flow-sediment feedbacks: the presence of vegetation modifies the spatial distribution of water flow, and thus sedimentation and erosion. Subsequently, changes to water flow, sedimentation, and erosion patterns affect the spatial pattern of vegetation establishment [5–7]. Understanding these vegetation-flow-sediment feedbacks is important to predict the outcomes of river management actions [8–10].

Recent research has improved the understanding of vegetation-flow-sediment feedbacks created by isolated, finite vegetation patches. Velocity declines 1 to 2 patch diameters ( $D$ ) upstream of the patch, as flow is diverted around the region of high drag caused by the presence of the vegetation [7, 11, 12]. The diversion of flow around the patch produces locally enhanced flow along the vegetation edge, which promotes erosion and may inhibit the lateral expansion of the patch, a negative feedback [8, 9, 13, 14]. Because the patches are porous, some flow penetrates through the patches into the wake, sometimes referred to as bleed flow. The bleed flow entering the wake delays the onset of the von Kármán vortex street until a distance  $L_1$  behind the patch. Over the distance  $L_1$  behind the patch, which we call the near wake region, the mean and turbulent velocity are depressed, relative to the free stream, and this encourages the deposition of fine sediment, creating conditions that favor new vegetation growth and thus patch expansion in the streamwise direction, a positive feedback [15, 16]. The formation of the von Kármán vortex street at the end of the  $L_1$  wake region significantly elevates the turbulence level, which may inhibit deposition. Beyond this point the velocity begins to recover back to the free stream value  $U_0$ .

Although several studies have contributed to the description of flow and deposition near an individual patch of vegetation, relatively few studies have investigated the interaction between two patches placed in close proximity to one another. The interaction between two developing wakes makes the flow field behind a pair of patches significantly more complex than that near a single patch. In the relatively simple case of two side-by-side circular patches separated by a gap, the flow is accelerated next to and in between the patches for all gap widths [7, 17]. This flow acceleration would tend to promote erosion and thereby inhibit the lateral growth of the patches. The wake in line with and immediately downstream of each individual patch is similar to that observed behind a single isolated patch, creating conditions that favor the deposition of fine material and, consequently, patch expansion in the streamwise direction in line with the individual patches [17]. Further downstream, the two wakes merge, producing a velocity minimum that promotes deposition on the centerline between the patches, but at some distance removed from the patches. Meire et al. [17] argue that this secondary deposition region may promote the growth of vegetation on the centerline between the patches, which in turn could diminish the flow between the patches, ultimately producing conditions favorable for the two patches to merge.

In this paper we build on the work of Meire et al. [17] by considering a wider range of two-patch configurations. In particular, the patch spacing was varied in both the transverse and longitudinal direction, denoted by  $T$  and  $L$ , respectively, as in Fig. 1. This is an important refinement, because in very few cases will the oncoming flow be perfectly aligned with the patches, i.e.  $L = 0$ , as assumed by Meire et al. [17]. A numerical model was used to explore how the patch spacing impacts the shape of the wake behind each patch, and the modeled velocity field was used to infer possible deposition and growth patterns. Using the results for pairs of patches, we infer how initial patch spacing might influence landscape development.

**Fig. 1** Definition sketch for two circular patches (grey circles) of equal diameter,  $D$ .  $L$  is the longitudinal spacing and  $T$  is the transverse spacing, both measured between the centers of each patch.  $U_0$  is the uniform inlet velocity set to  $9.5 \text{ cm s}^{-1}$  for these experiments



## 2 Modeling approach

This study considered emergent vegetation, for which flow diversion occurs predominantly in the horizontal plane. In particular, previous experimental studies using similar flow and patch configurations showed that three-dimensional effects associated with the bottom boundary-layer were of second order with regard to wake structure [18]. Subsequently, we have chosen a two-dimensional model, representing the streamwise and transverse coordinates, respectively (Fig. 1). In this study the  $x$ -axis pointed in the direction of flow with  $x = 0$  at the upstream edge of the patches, and the  $y$ -axis was in the transverse direction, with  $y = 0$  at the center of the transverse gap between the patches. The longitudinal ( $L$ ) and transverse ( $T$ ) spacing between the patches was measured between the patch centers. The velocity ( $u, v$ ) corresponded to  $(x, y)$ , respectively. The individual stems within a patch were represented by solid cylinders of diameter  $d$ , placed with stem density  $n$  [cylinders/cm<sup>2</sup>]. This produced a frontal area per volume of  $a = nd$ , and a solid volume fraction  $\phi = (\pi/4)ad$ .

Numerical experiments were carried out for 46 patch arrangements defined by eight different values of  $T/D$  between 1 and 8, and nine different values of  $L/D$  between 0 and 25. The specific combinations of  $T/D$  and  $L/D$  are shown in Fig. 2. Each patch had a diameter  $D = 22 \text{ cm}$ , and was composed of 45 rigid cylinders of diameter  $d = 1.2 \text{ cm}$  in a staggered arrangement, producing a solid volume fraction of  $\phi \approx 10 \%$  and a frontal area per volume  $a = 0.13 \text{ cm}^{-1}$ . The numerical experiments were conducted with  $U_0 = 9.5 \text{ cm/s}$ . To reduce the influence of the inlet, the upstream patch was placed  $3 \text{ m} (\approx 14D)$  downstream from the channel inlet. The computational flow domain chosen spans  $45D$  (to  $60D$ ) in the streamwise direction and  $20D$  in the spanwise direction. The blockage ratio,  $B$ , i.e., the ratio of the total obstructed width ( $2D$ ) to the channel width ( $W = 25D$ ) was 0.08. Since  $B \ll 1$ , the impact of the channel walls was low: preliminary simulations showed that, for channel widths of  $15D$  and  $20D$ , the difference in the velocity for any point was less than 5% (tested specifically for  $L/D = 0$  and  $T/D = 1.5$ ).

In order to provide a baseline for comparison, six simulations with a single patch were also performed. In these runs the center of the single patch was placed at the same position as the upstream patch within the pair. Specifically, single patch controls were located at  $x = 0.5D$  and  $y = 0.5D, 0.545D, 0.625D, 0.75D, 1D, \text{ and } 1.5D$ , corresponding to the two-patch cases  $T/D = 1, 1.09, 1.25, 1.5, 2, \text{ and } 3$ .

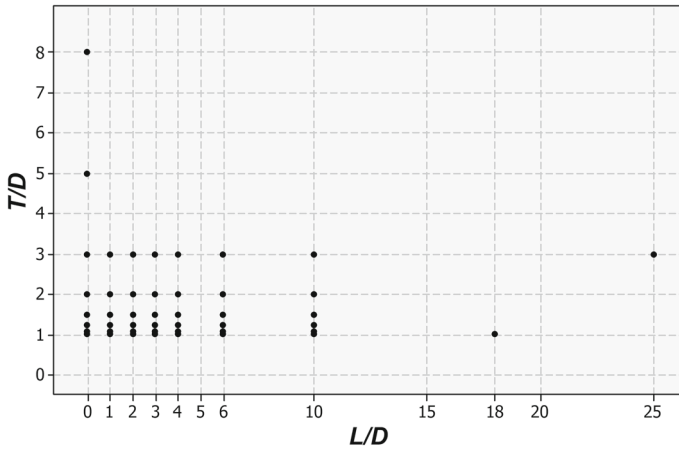


**Fig. 2** The 46 two-patch arrangements considered in this study. The center-to-center longitudinal spacing ( $L$ ) and transverse ( $T$ ) spacing were both varied

Simulations were carried out using the commercial computational fluid dynamics (CFD) code FLUENT<sup>®</sup>. This code uses the finite volume method for the spatial discretization of the domain. The governing equations are integrated over each control volume, such that mass and momentum are conserved, in a discrete sense, for each control volume. The simulations in this study were performed using the two-dimensional steady-state RANS (Reynolds Averaged Navier Stokes) equations with a  $k-\epsilon$  model.

Considering a steady flow of an incompressible and homogeneous fluid, the Reynolds-averaged equations for conservation of mass and momentum are given by:

$$\frac{\partial u_i}{\partial x_i} = 0$$

$$\frac{\partial u_j u_i}{\partial x_j} = -\frac{1}{\rho} \frac{\partial p}{\partial x_i} + \nu \frac{\partial^2 u_i}{\partial x_j \partial x_j} - \frac{\partial \overline{u'_i u'_j}}{\partial x_j}$$

where  $i$  or  $j = 1$  or  $2$ ;  $x_1$  and  $x_2$  denote the streamwise ( $x$ ) and cross-stream ( $y$ ) directions respectively;  $u_1$  and  $u_2$  are the corresponding mean velocity components (i.e.,  $u_1 = u$  and  $u_2 = v$ ).  $\overline{u'_i u'_j}$  is the Reynolds stress component, where  $u'$  denotes the fluctuating part of the velocity;  $p$  is the pressure; and  $\rho$  is the fluid density. For the calculation of the Reynolds stresses, the assumption of Boussinesq's approximation is used

$$\overline{u'_i u'_j} = \frac{\mu_t}{\rho} \left( \frac{\partial u_i}{\partial x_j} + \frac{\partial u_j}{\partial x_i} \right) - \frac{2}{3} k \delta_{ij}$$

where  $\mu_t$  is the turbulent viscosity,  $\delta_{ij}$  the Kronecker delta and  $k$  is the turbulent kinetic energy per unit mass, given by

$$k = \frac{1}{2} (\overline{u_1^2} + \overline{u_2^2})$$

Along with the Boussinesq approximation, the following definition of the eddy viscosity is used

$$\mu_t = \rho c_\mu \frac{k^2}{\epsilon}$$

where  $c_\mu$  is an empirical constant and  $\varepsilon$  is the energy dissipation rate given by the following equation

$$\varepsilon = \frac{k^{\frac{3}{2}}}{S}$$

where  $S$  is the length scale involved. The distributions of  $k$  and  $\varepsilon$  are calculated from the following transport equations

$$\begin{aligned} \frac{\partial \rho u_j k}{\partial x_j} &= \frac{\partial}{\partial x_j} \left( \frac{\mu_t}{\sigma_k} \frac{\partial k}{\partial x_j} \right) + G - \rho \varepsilon \\ \frac{\partial \rho u_j \varepsilon}{\partial x_j} &= \frac{\partial}{\partial x_j} \left( \frac{\mu_t}{\sigma_\varepsilon} \frac{\partial \varepsilon}{\partial x_j} \right) + c_1 \frac{\varepsilon}{k} G - \rho c_2 \frac{\varepsilon^2}{k} \end{aligned}$$

where  $G$  represents the generation of turbulence kinetic energy due to the mean velocity gradients

$$G = \mu_t \left( \frac{\partial u_i}{\partial x_j} + \frac{\partial u_j}{\partial x_i} \right) \frac{\partial u_i}{\partial x_j}$$

The standard values of the constants  $c_\mu = 0.09$ ,  $c_1 = 1.44$ ,  $c_2 = 1.92$ ,  $\sigma_k = 1.0$  and  $\sigma_\varepsilon = 1.3$  are used in the present computations.

As already mentioned, two-dimensional simulations were used in this study as they are able to capture the flow features that are important for the present goal. Fluent, CFD numerical code used in this study, use the finite control-volume method for the spatial discretization of the domain. Hence, in the two-dimensional simulations the volume is the computational domain in the  $xy$  plane multiplied by a unit depth (in the  $z$  direction). Pressure-velocity coupling was achieved in some simulations using the SIMPLE (Semi-Implicit Method for Pressure-Linked Equations) and in other simulations a combination of the SIMPLE and coupled pressure-based algorithms. In most of the cases, the simulations converged only using the SIMPLE method. In a few cases we changed from SIMPLE to coupled algorithm to reach the convergence of the solution. A second order upwind scheme was used for spatial discretization of the flow equations. Details of the governing equations, turbulence model, and algorithms can be found in the FLUENT<sup>®</sup> user's guide [19].

The full domain and zoomed-in views of the numerical grid for  $L/D = 1$  and  $T/D = 2$  are shown in Fig. 3. The grid had a finer spacing in regions of larger gradients (near the wall, the patch, and the wake) and coarser spacing in the regions of low velocity gradients. In addition, the grid was a block-structured grid composed of Cartesian H-grid blocks, which were uniform in the horizontal plane, and O-grid blocks, which were stretched towards the cylinders. The present meshing method has been previously applied with success for flows around cylinders (see, for example, Stoesser et al. [20]). A grid independency test was performed to ensure the quality of our CFD simulations. Three progressively finer grids were employed: a coarser grid, with 799,600 elements; a medium grid, with 1,131,000 elements; and a fine grid, with 1,605,000 elements.

The cylinders in the patch were arranged in a square array. The array was drawn inside a circle with diameter of 22 cm that represents the boundary of the patch. The array has a square form divided into 49 ( $7 \times 7$ ) smaller squares each 3 cm  $\times$  3 cm. The small squares in the array were filled with the stems. The stems and small squares are all concentric. Finally the 45 stems were placed symmetrically in the array and for this reason there are no stems at the array corners (See Fig. 3c).

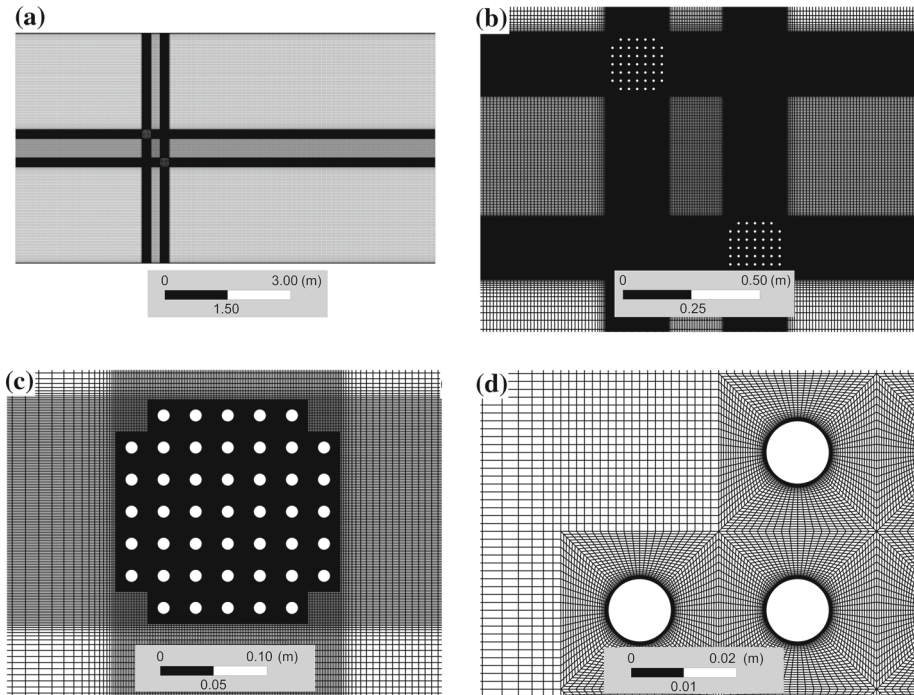


**Fig. 3** Computational grid for the  $L/D = 1$  and  $T/D = 2$  case: **a** entire computational domain; **b** close-up view near the 2 patches; **c** close-up view near one patch; and **d** close-up view near the cylinders

Boundary conditions were defined at the borders of the computation domain. A uniform flow was imposed at the inlet, with streamwise velocity  $u = U_0$  and transverse velocity  $v = 0$ . At the outlet an average static reference pressure of 0 Pa was specified. The zero-pressure outlet boundary condition has been widely used to calculate the flow around bluff bodies (see e.g. Tian et al. [21]). A no-slip boundary condition was applied at the cylinder edges and the channel walls. Symmetry conditions were applied at the bottom and the surface of the channel.

The numerical model was validated using experimental measurements near a single patch in a laboratory channel [12]. The simulations represented a 10 m long and 1.2 m wide channel with imposed inflow velocity  $U_0 = 9.5$  cm/s. A single circular patch of diameter  $D = 22$  cm was placed 3 m downstream from the channel entrance. To simplify the computational mesh, the computational cylinders were arranged into a square array, rather than a circular array used by Zong and Nempf [12]. This simplification is justified by experiments carried out by Vandenbruwaene et al. [7], who found that the flow field near square and circular arrays of the same diameter and stem density were very similar. The computational patch had 35 rigid cylinders ( $n = 0.1$  cylinders  $\text{cm}^{-2}$ ) of diameter 0.6 cm, producing a solid volume fraction of  $\phi \approx 0.03$ , which is the same used by Zong and Nempf [12]. The frontal area per volume was  $a = nd \approx 0.06 \text{ cm}^{-1}$ . Streamwise profiles of time-mean velocity along the centerline of the patch show that the maximum difference between numerical and experimental results was 6 % of the experimental measurement (Fig. 4). Figure 4 reveals that all three grid predictions were similar. Due to the limitation of available computational time, the coarse mesh was selected. It is important to note, as observed from comparison between experimental and numerical

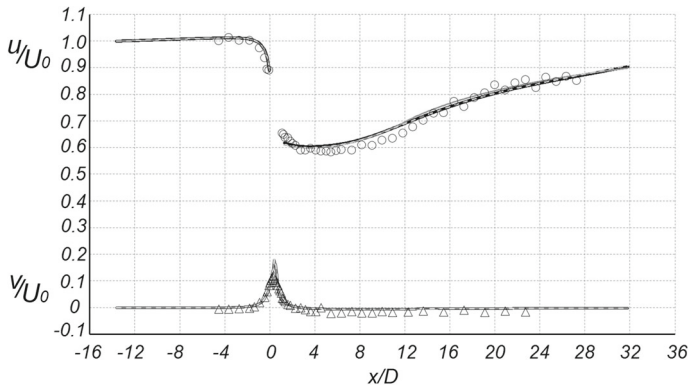


**Fig. 4** Comparison of the simulated time-mean streamwise velocity ( $u$ ) along the centerline of the patch and transversal velocity ( $v$ ) along the line  $y = D/2$  with the experiment of Zong and Nepf [12], *open circles* and *open triangles* for  $u$  and  $v$ , respectively. The boundaries of the patches lies between  $0 < x/D < 1$ . The maximum difference between numerical and experimental results was 6%. In both the numerical and physical experiment, the patch width was  $D = 22$  cm, and the patch solid volume fraction was  $\phi = 0.03$ . Coarse grid, with 799,600 elements (*solid black lines*); medium grid, with 1,131,000 elements (*solid gray lines*); fine grid, with 1,605,000 elements (*dashed gray lines*)

results in Fig. 4, that the most significant steady wake characteristics can be captured with a steady RANS simulation.

Regions of deposition are commonly associated with regions of diminished velocity [17,22]. For example, the effect of velocity on deposition is illustrated by Hjulström’s diagram [23], which relates deposition to velocity and particle size. Sediment is deposited when the velocity falls below the minimum velocity required to keep the particle in motion, which we call the threshold velocity. The threshold velocity is a function of sediment size, with smaller values associated with smaller grains. We used the threshold velocity to define the regions within which enhanced deposition would occur in the wake of the individual patches and patch pairs. Recognizing that the threshold velocity will depend on sediment size, we considered two thresholds,  $u/U_0 < 0.7$  and  $0.5$ , representing coarser and finer material, respectively. Although we cannot connect these velocities to specific sediment sizes, they provide an exploratory test of how threshold velocity impacts the areal extent of enhanced deposition. In addition, the higher threshold ( $u/U_0 < 0.7$ ) is correlated with the regions of enhanced net deposition observed in both Chen et al. [16] and Meire et al. [17].

### 3 Results and discussion

#### 3.1 Flow pattern around a single patch

The velocity distribution for a single patch ( $D = 22$ cm,  $a = 0.13$  cm<sup>-1</sup>) is shown in Fig. 5. The diversion of flow began at  $L_0 = 1.45D$  upstream of the patch, with  $L_0$  defined as the distance upstream of the patch at which  $\left| \frac{\partial(u/U_0)}{\partial(x/D)} \right| > 0.05$ , which is consistent with results presented in Rominger and Nepf [11] of  $L_0 = 2.0 (\pm 0.4) D$  and Zong and Nepf [12] of  $L_0 \approx 1D$ . The diversion of flow away from the vegetation patch led to acceleration along the vegetation edge, which is apparent in Fig. 5 as lobes of lighter shading on each side of the patch. Flow continued to divert laterally even within the patch, resulting in an area of

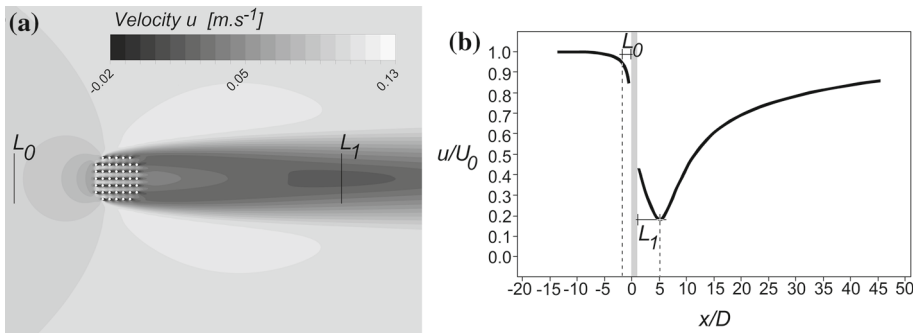


**Fig. 5** **a** Contour map of streamwise velocity ( $u$ ) for a single patch of diameter  $D = 22\text{cm}$ ,  $a = 0.13\text{ cm}^{-1}$  and flow blockage  $aD = 2.86$ . The center of the patch is at  $x = 0.5D$ ,  $y = 0.75D$ ; **b** streamwise velocity ( $u$ ) along the patch centerline noting the length-scales  $L_0$  and  $L_1$

low velocity directly behind the patch, consistent with previous studies [9, 16]. The velocity directly downstream of the patch was  $U_e = 0.40U_0$ .

There was no recirculation zone behind the patch (specifically, no region of negative velocity), which is in agreement with Chen et al. [16], who note that there is no recirculation zone behind low-flow blockage patches ( $C_{Da}D < 4$ ).

The region of low velocity behind the patch separated two regions of enhanced velocity, creating a shear layer on either side of the wake. The region of diminished velocity was maintained over a distance  $L_1$  measured from the back of the patch. The wake length,  $L_1$ , was defined as the distance along the patch centerline from the end of the patch to the point where the velocity began to increase. The dimensionless wake length obtained for our simulations was  $L_1/D \approx 4.1$ .

### 3.2 Flow pattern around two patches

The presence of a neighboring patch changes the wake structure, relative to that observed for an isolated patch (discussed in 3.1). We used the wake length,  $L_1$ , to explore the influence of a neighboring patch for different lateral ( $L$ ) and transverse ( $T$ ) distances (Fig. 6). The superscripts  $u$  and  $d$  indicate, respectively, the upstream patch ( $L_1^u$ ) and the downstream patch ( $L_1^d$ ). The value for an isolated, single patch will remain as  $L_1$ . Three different patterns for  $L_1$  were identified, depending on the patch spacing,  $L/D$  and  $T/D$ : (i) single patch behavior, in which each of the two patches produced a wake that was close to that produced by a single, isolated patch. This behavior was defined by the following limits:  $0.9 \leq L_1^u/L_1^d \leq 1.1$ ,  $0.9 \leq L_1^u/L_1 \leq 1.1$  and  $0.9 \leq L_1^d/L_1 \leq 1.1$ ; (ii) biased flow behavior, in which the lengths of the two wakes differed by more than 10 % ( $0 \leq L_1^u/L_1^d \leq 0.9$ ); (iii) diminished wake behavior, in which the lengths of the two wakes are equal, but smaller than the length behind an isolated patch ( $0.9 \leq L_1^u/L_1^d \leq 1.1$  and  $L_1^u/L_1 \leq 0.9$  and  $L_1^d/L_1 \leq 0.9$ ). These three flow patterns are now examined in more detail.

### 3.3 Flow pattern around side-by-side patches, $L/D = 0$

Figure 6a, b shows  $u$ -velocity distributions for two cases ( $T/D = 3$ ;  $T/D = 1.09$ ) in a side-by-side arrangement ( $L/D = 0$ ). The upstream adjustment length ( $L_0$ ) was a weak function of lateral spacing,  $T$ , with  $L_0 = 1.92D$  for  $T/D = 1.09$  and  $L_0 = 1.44D$  for

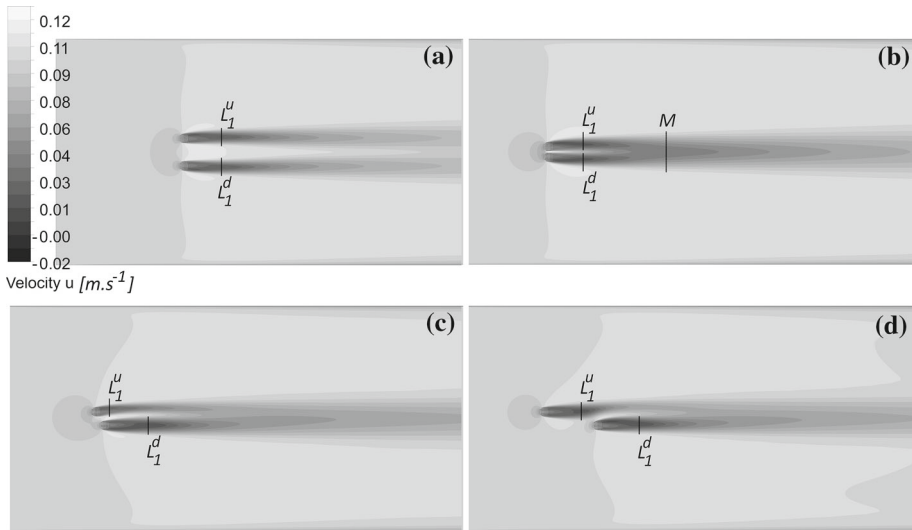


**Fig. 6**  $u$ -velocity contours for **a**  $L/D = 0$ ,  $T/D = 3$  (single patch behavior); **b**  $L/D = 0$ ,  $T/D = 1.09$  (diminished wake behavior); **c**  $L/D = 1$ ,  $T/D = 1.5$  (biased flow behavior); **d**  $L/D = 6$ ,  $T/D = 1.5$  (biased flow behavior).  $M$  marks the longitudinal position at which the two wakes merge into one, as indicated by a velocity minimum in the longitudinal transect along the centerline between the two patches ( $M$  could be only defined for the case in Fig. 6b)

$T/D = 2$ . Recall that  $L_0/D = 1.45$  for single, isolated patch (Fig. 5). The values of  $L_0$  observed for these side-by-side arrangements were close to those measured by Meire et al. [17] of  $L_0 = 1.7 (\pm 0.2) D$  over a range of spacing ( $T/D = 1$  to  $1.6$ ,  $L/D = 0$ ). Further, the values of  $L_0$  observed for the side-by-side arrangement agreed within uncertainty with Rominger and Nepf [11], who observed  $L_0 = 2.0 \pm 0.4 D$  for individual patches. Thus, although our simulation suggested that  $L_0$  increased by 30 % as the spacing decreased to nearly zero ( $T/D = 1.09$ ), the values were all within the range observed for isolated patches, which suggests that there was no upstream interaction, i.e. the presence of a neighboring patch did not significantly alter the distance upstream at which flow begins to adjust to each patch.

For  $L/D = 0$ , the flow pattern was symmetric about  $y = 0$  such that the near wake length-scale ( $L_1$ ) behind each patch was the same (Fig. 6a, b), but in these two cases was smaller than that observed for an isolated patch ( $L_1/D = 4.1$ ), which we call diminished wake behavior. In addition,  $L_1$  was a function of patch-spacing  $T$ . Specifically,  $L_1/D = 3.40$  at  $T/D = 1.09$  and  $L_1/D = 3.75$  at  $T/D = 3.0$ , i.e. as the patch-spacing increased the wake length-scale approached that of an isolated patch, which makes physical sense. The parameter range ( $T/D$ ) on which diminished wake behavior occurs is discussed in more detail below.

The result that  $L_1$  was shortened in a side-by-side configuration ( $L/D = 0$ ) differed from Meire et al. [17], who observed that  $L_1$  for a pair of side-by-side patches was not significantly altered from that of an isolated patch. This difference may be explained by the resolution of the Meire measurements. In the Meire study the longitudinal distance between measurement points was  $0.55D$ , a distance that roughly encompasses the variation observed in this study ( $3.4D$  to  $4.1D$ ). Finally, for  $L/D = 0$  flow acceleration between the patches was always present, even for  $T/D = 1$ , which is consistent with both Meire et al. [17] and Vandenbruwaene et al. [11].

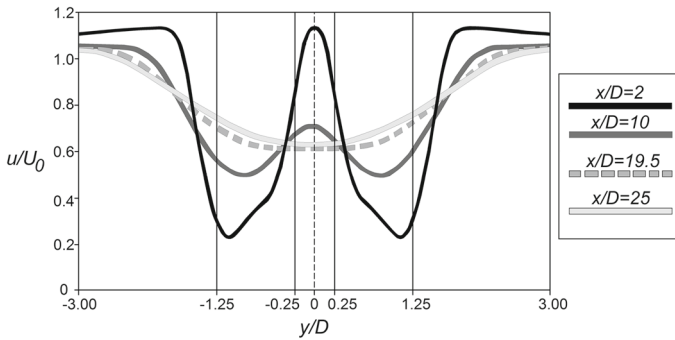


**Fig. 7** Lateral profiles of streamwise velocity ( $u$ ) for  $T/D = 1.5$ , and  $L/D = 0$  (side-by-side configuration). The *dashed, vertical line* indicates the centerline between the patches ( $y = 0$ ), and the *solid vertical lines* represent the edges of the patches. At  $x/D = 2$  and  $10$ , two distinct wakes were visible, with minimum velocity aligned with the centerline of each patch. At  $x/D = 19.5$  and  $25$  the individual wakes have merged to form a wake that resembles that of a single object of total width ( $D + L$ ), with a minimum velocity at the centerline between the two patches ( $y = 0$ )

Downstream from a pair of side-by-side patches, the flow field evolved in the streamwise direction from two side-by-side wakes to a single merged wake (e.g.  $L/D = 0$ ,  $T/D = 1.5$ , Fig. 7). Close to the patch pair (e.g.  $x/D = 2$ ) the profile showed two distinct wakes with local minimum velocity in-line with the individual patches and a maximum velocity on the centerline between the patches ( $y = 0$ ). Farther downstream ( $x/D > 2$ ), the centerline ( $y = 0$ ) velocity declined as the individual wakes merged, reaching the form of a single wake at  $x/D = 19.5$ . At this point, which we call the merging point  $M$ , the centerline velocity reached a minimum. Beyond this point ( $x/D \geq 19.5$ ) the wake resembled that of a larger, single patch of scale  $(D + L)$  with the minimum velocity in the lateral transect occurring at the centerline between the two patches. The wake merger ( $M$ ) and centerline minimum velocity occurred closer to the patches as patch lateral space ( $T/D$ ) decreased, consistent with the observations of Meire et al. [17]. For example, the wake merger position ( $M$ ) is visible within the frame for  $T/D = 1.09$  (Fig. 6b), but occurs beyond the end of the frame for  $T/D = 3$  (Fig. 6a). The merger position ( $M$ ) and associated centerline velocity minimum have been shown experimentally to promote a local region of enhanced deposition on the centerline between the two patches.

### 3.4 Flow pattern around two staggered patches, $L/D > 0$

Figure 6c, d illustrate two staggered configurations ( $L/D > 0$ ). When the neighboring patches were staggered, the flow through the gap between the patches was deflected laterally toward the upstream patch, and this cut off the wake development of the upstream patch. As a result, the wake length of the upstream patch ( $L_1^u$ ) was smaller than that for an isolated patch ( $L_1$ ). The wake behind the downstream patch was essentially the same as an isolated patch (within 10 %). As  $L/D$  increased, the deflection of gap flow decreased, and the upstream wake lengthened ( $L_1^u$  increased), until at  $L/D = 6$ , the upstream and downstream values for  $L_1$  were equal within 10 %. This suggests that a downstream patch that occurs within  $6D$  of an upstream neighbor can produce a negative feedback for the upstream patch by diminishing the length of the near wake, from which we infer the length-scale of enhanced deposition and potential growth will also be diminished.

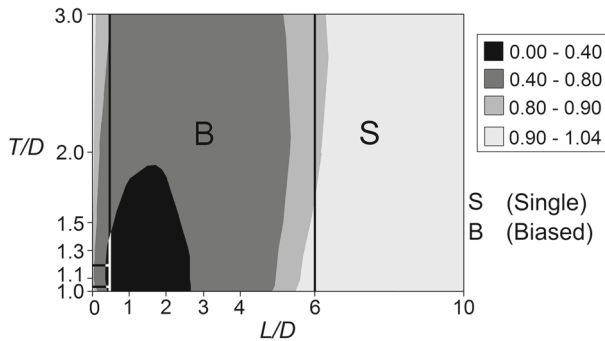


**Fig. 8** Ratio of upstream to downstream wake length-scale,  $L_1^u/L_1^d$ , as a function of  $L/D$  and  $T/D$ . Regions of biased flow behavior (B) and single patch behavior (S) are marked. The boundaries were drawn at the half distance between simulated values of  $L/D$  and  $T/D$ . The diminished wake behavior was only observed for side-by-side patches ( $L/D = 0$ ) over the range  $T/D = 1.09$  to  $1.25$ . For  $L/D = 0$ ,  $T/D > 1.25$ , single patch behavior was observed

The variation in the wake length-scale ratio  $L_1^u/L_1^d$  over the full range of lateral ( $L/D$ ) and transverse ( $T/D$ ) spacing is shown in Fig. 8. These values were used to define the classes of wake behavior, as discussed in the previous paragraphs. In particular, the biased flow (B) and single patch (S) behavior is noted in Fig. 8 with boundaries drawn at half the distance between the simulated values of  $L/D$  or  $T/D$  at which the transition was observed. We first consider the side-by-side configurations with  $L/D = 0$ . If the patches were spaced sufficiently far apart ( $T/D > 1.25$ ), they behaved as two independent patches, with  $L_1$  of each patch comparable to that of an isolated patch, i.e. single patch behavior. If the patches were at an intermediate spacing ( $1.09 \leq T/D \leq 1.25$ ), the lengths of the two wakes are equal, but smaller than the length behind a single patch (diminished wake behavior). If the patches were touching ( $T/D = 1$ ), single patch behavior was again observed ( $L_1^u = L_1^d = L_1$ ).

For  $L/D > 0$ , when the patches were far from one other ( $L/D > 6$ ), they exhibited single patch behavior (marked *S* in Fig. 8), i.e. there was no influence between the patches and  $L_1^u = L_1^d = L_1$ . If the patches were closer ( $0 < L/D < 6$ ), biased flow occurred and the upstream wake was significantly shorter than the downstream wake and decreased in length as the spacing ( $L/D$ ) decreased. The minimum value of  $L_1^u/L_1^d = 0$  (i.e. the upstream patch had no near wake region) occurred for  $L/D = 1$  and  $T/D = 1$  to  $1.25$ .

### 3.5 Implied deposition pattern

This section explores the possible influence of the velocity field on deposition patterns by delineating regions of potential net deposition based on two velocity thresholds,  $u/U_0 < 0.5$  and  $0.7$ . The potential deposition area was defined as the area within which the local velocity was below the chosen threshold. The deposition area for a single patch,  $A_1$ , for  $u/U_0 < 0.5$  and  $0.7$ , was  $9.9D^2$  and  $22.7D^2$ , respectively, and was not a function of patch position (Fig. 9). These areas will be used as the reference values as we explore the interaction of two patches.

For pairs of patches, the deposition area behind the upstream and downstream patch was denoted  $A_u$  and  $A_d$ , respectively, and the sum was defined as  $A_2 = A_u + A_d$ . Different deposition patterns were identified from the simulations, corresponding to the different flow patterns identified above. First, for single patch flow behavior, both patches have the same (within a 10 % margin) deposition area as an isolated patch. That is,  $0.9 \leq A_u/A_1 \leq$



**Fig. 9** The deposition area for a single patch ( $A_1$ ) is identified by the *black color* for two threshold velocities: **a**  $u/U_0 < 0.7$ ,  $A_1 = 22.7D^2$ ; **b**  $u/U_0 < 0.5$ ,  $A_1 = 9.9D^2$

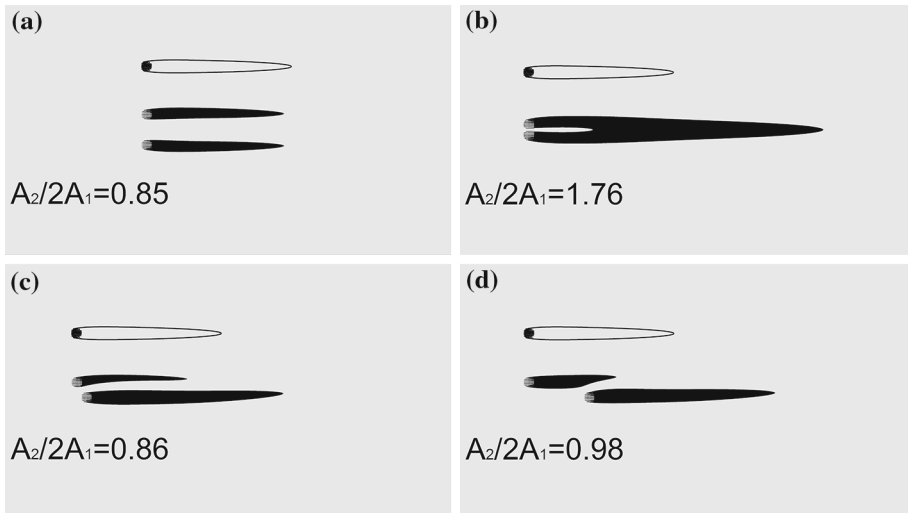


**Fig. 10** Deposition areas identified by the *black color* for  $u/U_0 < 0.5$ .  $A_1$  is the deposition area produced by an isolated patch and  $A_2$  is the total deposition area created with two patches. **a**  $L/D = 0$ ,  $T/D = 3$ ; **b**  $L/D = 0$ ,  $T/D = 1.09$ ; **c**  $L/D = 1$ ,  $T/D = 1.5$ ; **d**  $L/D = 6$ ,  $T/D = 1.5$ . Each subplot indicates the single-patch deposition area with an *open contour*. The total deposition area with two patches,  $A_2$ , is compared to that expected for two isolated patches ( $2A_1$ ). When  $A_2/2A_1 > 1$ , the neighboring patches provide a positive feedback to growth by creating a larger footprint of deposition than occurs for two isolated patches. When  $A_2/2A_1 < 1$ , the neighboring patches provide a negative feedback by diminishing the footprint of deposition, compared to two isolated patches

1.1;  $0.9 \leq A_d/A_1 \leq 1.1$ . This deposition pattern occurred when the two patches were far apart, so that no interaction between the two patches occurred, resulting in a single deposition zone behind each patch with an area the same as an isolated patch ( $A_2/2A_1 \approx 1$ ). In this case, the presence of a neighboring patch produced no feedback.

Second, when the two patches were located side-by-side ( $L/D = 0$ ), the deposition area behind each patch was equal (within 10 %). Two types of deposition pattern were observed: with a secondary deposition zone (Figs. 10b, 11b) and without a secondary deposition zone (Figs. 10a, 11a). In both cases the total deposition area with two patches ( $A_2$ ) was different from that of two isolated patches ( $A_2/2A_1 \neq 1$ ). When there was no secondary deposition zone (Figs. 10a and 11a), the deposition area of the two patches were equal, but less than the area behind a single patch, so that  $A_2/2A_1 < 1$ . Neighboring patches in this configuration produced a negative feedback, because a neighboring patch diminished the overall deposition, compared to two isolated patches. When a secondary deposition zone was present, the total

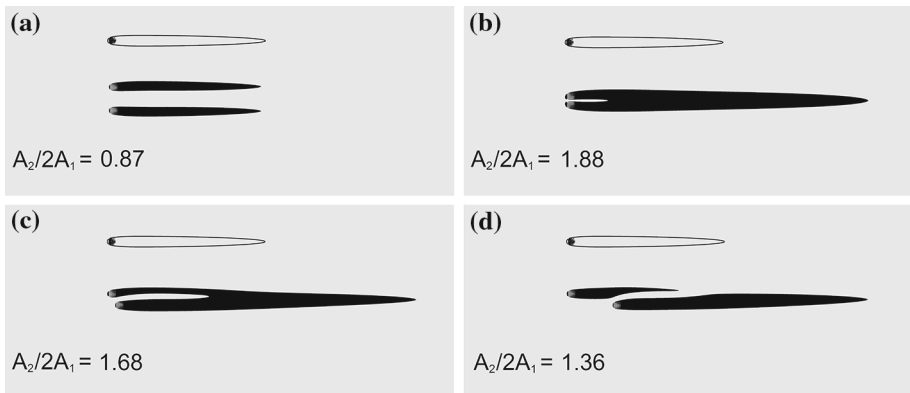


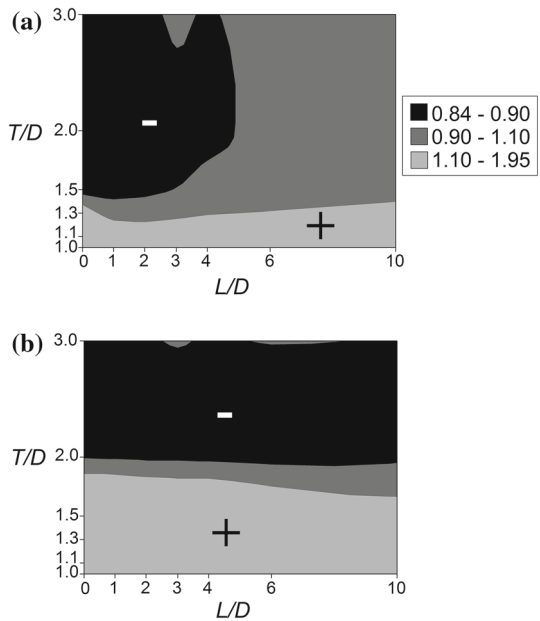
**Fig. 11** Deposition areas identified by the *black color* for  $u/U_0 < 0.7$ .  $A_1$  is the deposition area produced by an isolated patch and  $A_2$  is the total deposition area created with two patches. **a**  $L/D = 0$ ,  $T/D = 3$ ; **b**  $L/D = 0$ ,  $T/D = 1.09$ ; **c**  $L/D = 1$ ,  $T/D = 1.5$ ; **d**  $L/D = 6$ ,  $T/D = 1.5$ . Each subplot indicates the single-patch deposition area with an open contour. The total deposition area with two patches,  $A_2$ , is compared to that expected for two isolated patches ( $2A_1$ ). When  $A_2/2A_1 > 1$ , the neighboring patches provide a positive feedback to growth by creating a larger footprint of deposition than occurs for two isolated patches. When  $A_2/2A_1 < 1$ , the neighboring patches provide a negative feedback by diminishing the footprint of deposition, compared to two isolated patches

deposition area of the two patches was greater than two individual patches ( $A_2/2A_1 > 1$ , Figs. 10b and 11b). Neighboring patches in this configuration provided a positive feedback, because the neighboring patch enhanced the overall deposition and potential for new growth. The leading edge of the secondary deposition zone moved closer to the patches as  $T$  decreased, consistent with the experimental deposition patterns obtained by Meire et al. [17]. As suggested by Meire et al. [17], if the zones of secondary deposition promote growth, the new vegetation on the centerline could block flow on the centerline, eventually leading to a merger of the original patches into a larger vegetated structure.

Third, for cases with biased flow behavior, two deposition patterns were observed: with a secondary deposition zone (Fig. 11c) and without a secondary deposition zone (Figs. 10c, d, 11d). In the later case (Fig. 11d), the deposition zone behind the upstream patch was smaller than that behind an isolated patch ( $A_u < A_1$ ), so that the downstream neighbor provided a negative feedback to growth for the upstream patch. In contrast, there was an increase in deposition area behind the downstream patch compared to a single patch ( $A_d > A_1$ ), i.e. an upstream neighbor enhanced (positive feedback) the growth potential of the downstream patch.

Figure 12 summarizes the tendencies for positive (light grey) and negative (black) feedbacks associated with different patch-to-patch spacing for both velocity thresholds. We first consider the  $u/U_0 < 0.5$  threshold (top subplot). For the side-by-side configurations ( $L = 0$ ), unless the patches were nearly touching ( $T/D < 1.5$ ), neighboring patches produced a negative feedback ( $A_2/2A_1 < 0.9$ ). The negative feedback was observed for lateral spacing as large as  $T/D = 8$ , but for larger spacing we expect the deposition to return to single-patch behavior ( $A_2/2A_1 = 1.0 \pm 0.1$ ). On the other hand, when the patches had a small lateral spacing ( $T/D < 1.3$ ), a positive feedback ( $A_2/2A_1 > 1.1$ ) was observed for all longitudinal spacing considered (grey region along  $x$ -axis). The maximum feedback ( $A_2/2A_1 = 1.95$ ) occurred at ( $L/D = 0$ ,  $T/D = 1$ ). For patches separated by more than  $L/D = 5$  and  $T/D = 1.5$ , there was no feedback, and the deposition area was essential that same as that

**Fig. 12** Dependence on  $L/D$  and  $T/D$  of the nondimensional deposition area,  $A_2/2A_1$  for deposition defined by two velocity thresholds: **a**  $u/U_0 < 0.5$ ; **(b)**  $u/U_0 < 0.7$ . The plus (“+”) and minus (“-”) signs indicate, respectively, positive and negative feedbacks due to the presence of a neighboring patch



produced by two isolated patches ( $A_2/2A_1 = 1.0 \pm 0.1$ , medium grey region in Fig. 12a). When we considered a higher threshold velocity ( $u/U_0 < 0.7$ , Fig. 12b), both the positive and negative patch interactions became stronger, i.e. positive and negative feedbacks both occurred over a larger  $L - T$  parameter space. The expansion of the positive feedback region occurred because with a higher threshold velocity weaker patch interactions are needed to depress the velocity below this threshold, and these weaker interactions can occur at larger patch spacing. The enlargement of the negative feedback parameter space is related to the fact that the deposition area of an isolate patch ( $A_1$ ) increases (due to a higher threshold velocity), shifting the ratio  $A_2/2A_1$ . Recognizing that a smaller threshold velocity is associated with smaller grain size, the comparison between Fig. 12a, b suggests that patch-interaction has a weaker impact on finer suspended loads.

To further illustrate the different feedbacks observed for the upstream and downstream patches, Fig. 13 shows the dependence on  $L/D$  and  $T/D$  of the nondimensional upstream deposition area,  $A_u/A_1$ , and the nondimensional downstream deposition area,  $A_d/A_1$ , for the  $u/U_0 < 0.5$  threshold. We can only discuss the lower threshold velocity, because for  $u/U_0 < 0.7$ , the secondary deposition zones often merged with the primary deposition zones, making it impossible to define  $A_u$  and  $A_d$  separately for all  $T/D$  and  $L/D$  arrangements. We particularly focus on the feedbacks for staggered patch configurations ( $L/D \geq 1$ ). Due to the biased flow described in Sect. 3.4, the deposition zone of the upstream patch was always diminished, relative to an isolated patch, with the greatest reduction ( $A_u/A_1 = 0.24$ ) occurring at  $L/D = 1$ ,  $T/D = 1$  (Fig. 13a). As the longitudinal spacing ( $L$ ) increased, this negative feedback gradual declined and disappeared for  $L/D > \approx 8$ , i.e.  $A_u/A_1 = 1.0 \pm 0.1$  for  $L/D > 8$ . The deposition zone associated with the downstream patch was always enhanced, with maximum enhancement ( $A_d/A_1 = 2.79$ ) occurring for  $L/D = 1$  and  $T/D = 1$ . For patches with lateral spacing less than  $1.3D$ , the enhanced deposition area occurred for all longitudinal spacing considered. Notably, the positive feedback for the downstream patch extended over larger patch spacing than the negative feedback on the upstream patch.

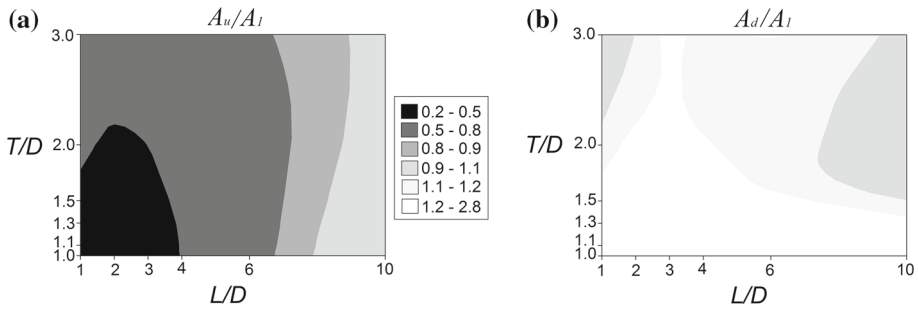


**Fig. 13** Nondimensional deposition area as a function of  $L/D$  and  $T/D$  for  $u/U_0 < 0.5$ : **a**  $A_u/A_1$ , nondimensional upstream patch deposition area; **b**  $A_d/A_1$ , nondimensional downstream patch deposition area

For patches with lateral spacing greater than  $1.5D$ , the feedback was eliminated at longitudinal spacing around  $L/D = 8$ , similar to the limit of influence on the upstream patch.

### 3.6 Implications for large-scale landscape evolution

This numerical study of two-patch interactions can provide some insight into large-scale landscape evolution. We specifically compared two scenarios, one for which the initial patch spacing was large enough to produce no patch-to-patch feedback, and one for which the initial patch-to-patch spacing was small enough to produced strong feedbacks. The initial state for the first scenario is shown in Fig. 14a. The longitudinal and transverse spacing between the patches was sufficient ( $T/D > 8$ ,  $L/D > 8$ ) to initially produce, a deposition zone similar to an isolated patch behind each individual patch (Fig. 14b). If the patches grew into these deposition regions, the individual patches lengthen, but do not widen. Meanwhile, due to flow diversion away from the patches, the flow between the patches is elevated, which inhibits patch expansion and maintains these bare regions (e.g. see discussion of the influence of bare regions in [17]). We conjecture that the patches will continue to grow only in the streamwise direction, eventually forming a landscape dominated by flow-parallel regions of vegetation and channel (Fig. 14c). This configuration is likely to be stable, because the high velocities in the bare adjacent areas inhibit expansion of vegetation into these zones. Thus, we conjecture that the vegetation will evolve to a state characterized by relatively stable channels and well-defined vegetated regions (with a width of the order of  $D$ ) (see Fig. 14c). The end pattern of this scenario is similar to observations from the field and previous numerical simulations. For example, Bernhardt and Willard [24] observed, in the Florida Everglades, a landscape characterized by longitudinally oriented ridges of vegetation and open-water sloughs (see Fig. 3 in [24]). Through process-based numerical modeling, Larsen and Harvey [6] have also reproduced a landscape with parallel preferential flow channels (see the category “Parallel Preferential Flow Channels” in [6], Fig. 1). Figure 14d presents an actual landscape from the Florida Everglades ( $26^{\circ}09'45.6''N$   $80^{\circ}40'21.9''W$ ), obtained from Google Maps, which closely resembles the final state proposed in Fig. 14c.

In the second scenario (Fig. 14e), the patches were initially placed close enough that patch-to-patch feedbacks would occur, specifically the initial patch spacing fell in the parameter space ( $L$ ,  $T$ ) for biased flow (Fig. 11) and negative feedbacks to the upstream patch (Fig. 13a).

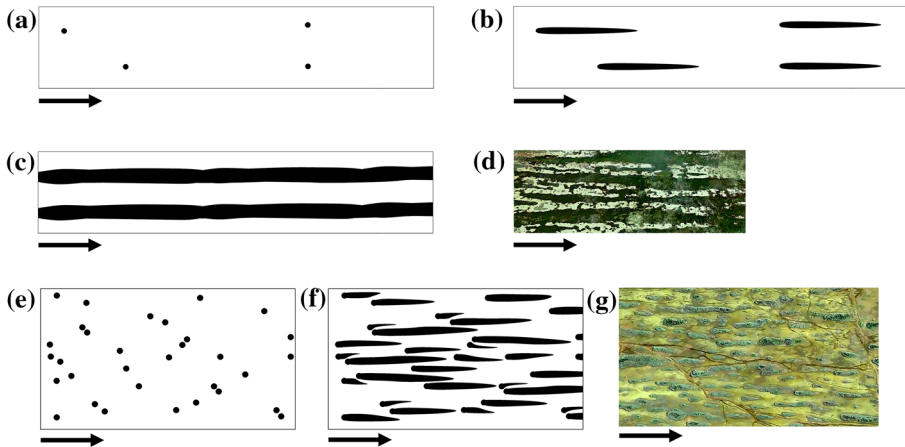


**Fig. 14** a–c. Evolution of a vegetated landscape starting from sparsely distributed pioneer vegetation. **a** Initial longitudinal and transverse spacing between the patches is sufficient to produce no patch-to-patch interaction. **b** Deposition area added behind each patch is the same as that behind an isolated patch **c** Conjectured final landscape characterized by relatively stable channels (bare regions) and well-defined vegetated regions. **d** A landscape ( $26^{\circ}09'45.6''\text{N } 80^{\circ}40'21.9''\text{W}$ ), obtained from Google Maps, which closely resembles conjectured landscape in (c). e–f. Evolution of a vegetated landscape starting from **e** closely distributed pioneer vegetation. The initial spacing is small enough ( $L/D < 6$ ) to limit the wake growth and deposition areas of each patch, yielding a distribution of small patches as a final state **f** characterized by elongated vegetation patches oriented parallel to the flow. **g** An actual landscape ( $26^{\circ}01'35.2''\text{N } 80^{\circ}50'19.1''\text{W}$ ), obtained from Google Maps, which closely resemble (f)

We assumed that the deposition behind each patch would depend only on the position of its nearest neighbor vegetation patch. For example, if patch A was located at  $x = 0$  and  $y = 0$  and the nearest downstream vegetation patch B was  $x = 6D$  and  $y = 1.5D$ , then the deposition area behind patch A was assumed to follow that observed numerically for a pair of patches separated by  $L/D = 6$  and  $T/D = 1.5$ , e.g. as shown in Fig. 11d. Letting the vegetation patches in Fig. 14e grow into their respective deposition areas yields the new landscape shown in Fig. 14f. The accelerated flow between the patches may limit further patch growth, so that the landscape evolves to a mosaic of small patches of different patch length, but generally elongated parallel to the flow. A distribution of patch sizes aligned preferentially to the flow (as shown in Fig. 14f) is consistent with observations of freshwater macrophyte distributions in a lowland river in Belgium [25] and in Scotland [26]. Larsen and Harvey [6] produced a similar landscape pattern within their landscape evolution model (see the category “Small Elongated Islands” in [6], Fig. 1). Finally, Fig. 14g presents an actual landscape from Florida Everglades ( $26^{\circ}01'35.2''\text{N } 80^{\circ}50'19.1''\text{W}$ ), obtained from Google Maps, which closely resemble our second scenario.

The two scenarios considered here highlight the potential role of initial patch spacing on landscape patterns. If pioneer vegetation is sparsely distributed (patch spacing larger than  $10D$ ), the feedback to deposition and additional plant growth may tend toward a channelled landscape (Fig. 14d). If the pioneer vegetation is densely distributed (patch spacing less than  $6D$ , based on Fig. 13), patch interaction tends to shorten the deposition zones, limiting patch expansion, resulting in a mosaic of patch sizes generally elongated in the streamwise direction (Fig. 14f).

## 4 Conclusions

This study examined the flow field and inferred deposition patterns around two nearby circular patches of vegetation using CFD. The following trends were observed for the threshold velocity  $u/U_o < 0.5$ . When the two patches were far from each other ( $L/D > 8$ ,  $T/D > 8$ ), wake interaction was weak and flow and deposition patterns around each patch resembled those of a single, isolated patch. When the two patches were close enough ( $L/D < 8$ ,  $T/D < 8$ ), both positive and negative feedbacks to wake scale and inferred deposition area were observed. For side-by-side patches ( $L/D = 0$ ), the total deposition area was enhanced (positive feedback) for small gaps ( $L/D < 1.5$ ) but diminished (negative feedback) for large gaps ( $T/D > 1.5$ , based on Fig. 12a). For staggered patches ( $L/D \geq 1$ ), the flow between the patches deflected laterally toward the upstream patch, which shortened the upstream patch wake and diminished its deposition area, relative to an isolated patch (negative feedback). The downstream patch in a staggered pair exhibited a positive feedback, with the wake length and deposition area both enhanced, relative to an isolated patch. The interaction between staggered patches may explain the landscape consisting of a distribution of small patch sizes generally aligned with the flow (Fig. 14g) which is often observed in rivers.

**Acknowledgments** Paulo H. S. de Lima wishes to acknowledge support given to him by National Council for the Improvement of Higher Education (CAPES/FUNDECT). Johannes G. Janzen wishes to acknowledge support given to him by National Council for Scientific and Technological Development (CNPq) through grant 246756/2012-8 and Federal University of Mato Grosso do Sul (UFMS).

## References

1. Kemp JL, Harper DM, Crosa GA (2000) The habitat-scale ecohydraulics of rivers. *Ecolog Eng* 16(1):17–29. doi:[10.1016/S0925-8574\(00\)00073-2](https://doi.org/10.1016/S0925-8574(00)00073-2)
2. Wilcock R, Champion P, Nagels J, Crocker G (1999) The influence of aquatic macrophytes on the hydraulic and physico-chemical properties of a New Zealand lowland stream. *Hydrobiologia* 416:203–214. doi:[10.1023/A:1003837231848](https://doi.org/10.1023/A:1003837231848)
3. Jones JI, Collins AL, Naden PS, Sear DA (2012) The relationship between fine sediments and macrophytes in rivers. *River Res Appl* 28:1006–1018
4. Pollen-Bankhead N, Simon A (2010) Hydrologic and hydraulic effects of riparian root networks on streambank stability: Is mechanical root-reinforcement the whole story? *Geomorphology* 116(3–4):353–362
5. Van De Wiel M, Couthard T, Macklin M, Lewin J (2007) Embedding reach-scale fluvial dynamics within the CAESAR cellular automaton landscape evolution model. *Geomorphology* 90:283–301
6. Larsen LG, Harvey JW (2011) Modeling of hydroecological feedbacks predicts distinct classes of landscape pattern, process, and restoration potential in shallow aquatic ecosystems. *Geomorphology* 126:279–296
7. Vandenbruwaene W, Temmerman S, Bouma T, Klaassen P, de Vries M, Callaghan D, van Steeg P, Dekker F, van Duren LA, Martini E, Balke T, Biermans G, Schoelynck J, Meire P (2011) Flow interaction with dynamic vegetation patches: Implications for biogeomorphic evolution of a tidal landscape. *J Geophys Res-Earth Surf* 116
8. Bennett S, Wu W, Alonso CV, Wang SY (2008) Modeling fluvial response to instream woody vegetation: implications for stream corridor restoration. *Earth Surf Process Landf* 33:890–909
9. Follett EM, Nepf HM (2012) Sediment patterns near a model patch of reedy emergent vegetation. *Geomorphology* 179:141–151
10. Neary VS, Constantinescu SG, Bennett SJ, Diplas P (2012) Effects of vegetation on turbulence, sediment transport, and stream morphology. *J Hydraul Eng* 138:765–776
11. Rominger JT, Nepf HM (2011) Flow adjustment and interior flow associated with a rectangular porous obstruction. *J Fluid Mech* 680:636–659
12. Zong L, Nepf HM (2011) Spatial distribution of deposition within a patch of vegetation. *Water Resour Res* 47:1–12. doi:[10.1029/2010WR009516](https://doi.org/10.1029/2010WR009516)

13. Bouma TJ, van Duren LA, Temmerman S, Claverie T, Blanco-Garcia A, Ysebaert T, Herman PMJ (2007) Spatial flow and sedimentation patterns within patches of epibenthic structures: combining field, flume and modelling experiments. *Cont Shelf Res* 27(8):1020–1045
14. Rominger JT, Lightbody AF, Nepf HM (2010) Effects of added vegetation on sand bar stability and stream hydrodynamics. *J Hydraul Eng* 136(12):994–1002
15. Tsujimoto T (1999) Fluvial processes in streams with vegetation. *J Hydraul Res* 37(6):789–803
16. Chen Z, Ortiz A, Zong L, Nepf H (2012) The wake structure behind a porous obstruction and its implications for deposition near a finite patch of emergent vegetation. *Water Resour Res* 48(9):18
17. Meire D, Kondziolka J, Nepf H (2014) Interaction between neighboring vegetation patches: impact on flow and deposition. *Water Resour Res* 50(5):3809–3825. doi:[10.1002/2013WR015070](https://doi.org/10.1002/2013WR015070)
18. Zong L, Nepf H (2012) Vortex development behind a finite porous obstruction in a channel. *J Fluid Mech* 691:368–391. doi:[10.1017/jfm.2011.479](https://doi.org/10.1017/jfm.2011.479)
19. Fluent Inc. (2014) User's guide (release 14.5.7)
20. Stoesser T, Kim SJ, Diplas P (2010) Turbulent flow through idealized emergent vegetation. *J Hydraul Eng* 136:1003–1017
21. Tian X, Ong M, Yang J, Myrhaug D (2013) Unsteady RANS simulations of flow around rectangular cylinders with different aspect ratios. *Ocean Eng* 58:208–216
22. Sand-Jensen K (1998) Influence of submerged macrophytes on sediment composition and near-bed flow in lowland streams. *Freshw Biol* 39(4):663–679
23. Christiansen EH et al (2014) *Dynamic Earth*. Jones & Bartlett Publishers, Burlington Print
24. Bernhardt CE, Willard DA (2009) Response of the Everglades' ridge and slough landscape to late Holocene climate variability and 20th century water-management practices. *Ecolog Appl* 19:1723–1738
25. Schoelynck J, De Groot T, Bal K, Vandenbruwaene W, Meire P, Temmerman S (2012) Self-organized patchiness and scale-dependent bio-geomorphic feedbacks in aquatic river vegetation. *Ecography* 35:760–768
26. Cameron SM, Nikora VI, Albayrak I, Miler O, Stewart M, Sniscalchi F (2013) Interactions between aquatic plants and turbulent flow: a field study using stereoscopic PIV. *J Fluid Mech* 732:345–372